ACADEMIA ROMÂNĂ
Revue Roumaine de Chimie
https://www.icf.ro/rrch/

Rev. Roum. Chim.,
2024, *69*(7–8), 365–373
DOI: 10.33224/rrch.2024.69.7-8.04

STRUCTURAL, PHYSICAL, MORPHOLOGICAL AND DIELECTRIC PROPERTIES OF Sm MODIFIED PZT-PMI BINARY CERAMICS

Malika ABBA,[a,*] Abdelhek MEKLID,[b] Adel KHIOUANI,[c] Salah Eddine HACHANI[d] and Rahima RAHAL[a]

[a] Laboratory of Molecular Chemistry and Environment, University of Biskra, BP 145, 07000, Biskra, Algeria
[b] Laboratory of Applied Chemistry, University of Biskra, BP 145, 07000 Biskra, Algeria
[c] Laboratory of Materials Chemistry and the Living: Activity & Reactivity, Department of Chemistry, Faculty of Matter Sciences, University of Batna-1. 05000, Algeria
[d] Department of Process Engineering & Petrochemistry, Faculty of Technology, University of El Oued, El Oued, 39000, Algeria

Received October 8, 2023

Solid solutions of $Pb_{1-x}Sm_x[Zr_{0.50}Ti_{0.45}(Mo_{1/3}In_{2/3})_{0.05}]_{1-x/4}O_3$, known as PSZT-PMI, were successfully synthesized using the mixed oxide method at high temperature. The concentrations of Sm^{+3} varied (x = 0.03, 0.08, 0.10, and 0.12). The resulting ceramic samples underwent sintering at 1250°C, followed by comprehensive analysis utilizing various laboratory techniques, including X-ray diffraction (XRD), scanning electron microscopy (SEM), density measurement, dielectric measurements, and Raman spectroscopy. The XRD analysis confirmed the crystallization of the ceramics in a tetragonal phase structure. Among the samples, the one with 8% Sm^{3+} exhibited the highest experimental density, measuring 92.6641%. Remarkably, this particular ceramic sample also demonstrated exceptional dielectric properties, characterized by a relative permittivity (ε_r) of 12503.59, a loss tangent (tanδ) of 0.04168, and a Curie temperature (T_c) of 635K. SEM micrographs revealed the presence of uniformly distributed grains with varying shapes and sizes across the entire surface of the samples.

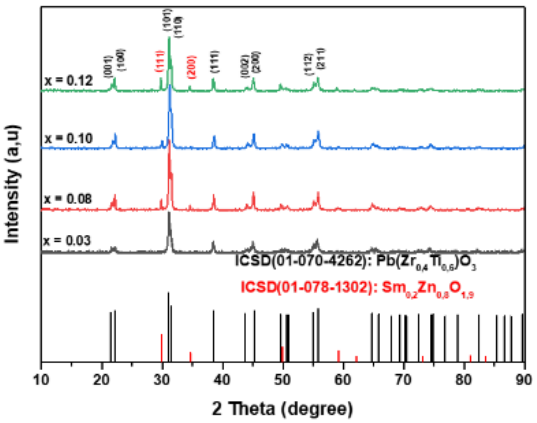

INTRODUCTION

The solid solution of $PbZr_{1-x}Ti_xO_3$, commonly referred to as lead zirconate titanate (PZT), has been extensively researched over the past four decades, primarily due to its exceptional dielectric, ferroelectric, and piezoelectric properties.[1–4] These ceramics exhibit a remarkable electromechanical response, which is most prominent at the morphotropic phase boundary (MPB). The MPB composition serves as a demarcation between the tetragonal phase (rich in Ti) and the rhombohedral phase (rich in Zr) fields, further enhancing the material's performance.

In practical applications of PZT, the incorporation of various impurities has been

* Corresponding author: m.abba@univ-biskra.dz

employed to enhance the piezoelectric and ferroelectric properties.[5,6] These additives can be broadly categorized into two groups: 'donor type' and 'acceptor type'. Noteworthy examples of the former group include Nb^{5+}, Ta^{5+}, and La^{3+}, whereas F^{e3+}, Mg^{2+}, and Al^{3+} belong to the latter group. Extensive research has demonstrated that the physical properties of PZT ceramics are highly sensitive to factors such as compositional variations, particle size, doping characteristics, calcination, and sintering temperature.[7–10]

The solid state reaction is a highly effective process employed for the production of PZT ceramics. This technique involves meticulously blending stoichiometric quantities of raw reagents, typically in the form of oxides, within a solvent medium such as acetone. Subsequently, the resulting mixture is subjected to thorough drying using an oven, followed by grinding in a mechanical mortar. Finally, the mixture is carefully calcined at an optimal temperature to achieve the desired ceramic phase.[11]

The integration of samarium Sm into PZT ceramics has become a focal point in recent research pursuits, drawing substantial attention for its potential impact. A seminal study brought to light the susceptibility of PZT based ceramics to localized structural modifications induced by rare earth (Sm) dopant at the A site.[12] In another remarkable exploration led by Li *et al*. emphasis was placed on the doping of PZT at the B site, yielding ceramics with extraordinary piezoelectric characteristics and robust ferroelectric properties. Notably, these ceramics showcased an impressive Curie temperature of 335 °C.[13] Adding depth to our understanding, Shi *et al*. delved into the effects of Li^+ and Sm^{3+} dopants on the properties of PZT ceramics. Their findings revealed that the ceramics under scrutiny exhibited resilient piezoelectric and ferroelectric properties, accompanied by a significantly elevated dielectric constant, thereby enriching our knowledge in this domain.[14]

On its part, the infusion of molybdenum into PZT ceramics has captivated the attention of researchers. In a comprehensive study, the piezoelectric PZT ceramic chips demonstrated both reasonable and feasible performance.[15]

In this original study, a comprehensive investigation was conducted to explore the potential enhancements in the properties through complex doping of multiple elements, as compared to single element donor or acceptor-doped PZT. Specifically, $Pb_{1-x}Sm_x[Zr_{0.5}0Ti_{0.45}(Mo_{1/3}In_{2/3})_{0.05}]_{1-x/4}O_3$ (referred to as PSZT-PMI) ceramics were synthesized by doping Sm^{3+} at the A site and introducing multiple ions (Mo and In) at the B sites of PZT ceramics. The research focused on analyzing the crystal structure, volume distribution of particle size, density, and porosity of PSZT-PMI ceramics with varying values of x (0.03, 0.08, 0.10, and 0.12). The compositions were prepared using a high temperature solid state reaction technique. The stoichiometric compositions formulas of the studied samples are presented in Table 1.

Table 1

Stoichiometric compositions formulas of the studied samples

x [%]	Formula
3	$Pb_{0.97}Sm_{0.03}[Zr_{0.50}Ti_{0.45}(Mo_{1/3}In_{2/3})_{0.05}]_{0.9925}O_3$
8	$Pb_{0.92}Sm_{0.08}[Zr_{0.50}Ti_{0.45}(Mo_{1/3}In_{2/3})_{0.05}]_{0.98}O_3$
10	$Pb_{0.9}Sm_{0.10}[Zr_{0.50}Ti_{0.45}(Mo_{1/3}In_{2/3})_{0.05}]_{0.975}O_3$
12	$Pb_{0.88}Sm_{0.12}[Zr_{0.50}Ti_{0.45}(Mo_{1/3}In_{2/3})_{0.05}]_{0.97}O_3$

EXPERIMENTAL

Samples Elaboration

To synthesize the desired ceramics, a conventional mixed oxide processing method was employed. Industrial-grade raw powders of PbO (99%), ZrO_2 (99%), TiO_2 (99%), Sm_2O_3 (99%), MoO_3 (99%), and In_2O_3 (99%) were utilized. The powders were dispersed in acetone and mixed using a magnetic stirrer for 4 hours. The resulting paste was dried at 80°C, followed by crushing in a glass mortar for 4 hours. Calcination of the powders took place at 900 °C for 240 minutes with a heating rate of 2 °C/min. The calcined powders were crushed again, this time for 6 hours, to achieve better agglomerate size reduction. A 5% polyvinyl alcohol (PVA) water solution was used as a binder to enhance the powders' plasticity, with a weight ratio of 1:20 between the PVA solution and the powders. The mixture of powder and PVA solution was then uniaxially pressed into pellets using a hydraulic press with a pressure of 3 000 kg/cm³. The resulting pellets had a diameter of 13 mm and a thickness of 1 mm. To prevent excessive lead evaporation during sintering, the pellets were packed into covered alumina crucibles filled with $PbZrO_3$ powders. Sintering was

performed by heating the crucibles at a rate of 2 °C/min to 1250 °C for 240 minutes, followed by natural cooling in the furnace.

Samples characterization

The prepared powders were investigated using several laboratory techniques. X-ray diffraction analysis was carried out using a BRUKER-AXE D8 diffractometer with CuKα radiation (λ = 1.5406 Å) in the range of Bragg angles from 10° to 90° at a scanning rate of 2°/min. The density of the sintered pieces was calculated based on their dimensions and weights.

The cell parameters and the volume corresponding to the studied PSZT-PMI were meticulously derived through precise calculations utilizing diffraction angles (2θ) and interreticular distances d_{hkl} provided directly by the X'pert HighScore software, employing the Bragg relation. The determination of these parameters involved applying the expression for the interreticular distance d_{hkl} as a function of the tetragonal phase parameters *a*, *b*, *c*, α, β, γ (where $a = b \neq c$; α = β = γ). The mathematical representation of the interreticular distance d_{hkl} is expressed as follows:

$$d_{hkl} = \frac{1}{\sqrt{(1/a)^2(h^2 + k^2) + (1/c)^2 l^2}}$$

For the specific case of the two hkl planes (200) and (002) within the tetragonal system, the derived parameters are as follows:

$$a = 2d_{200}$$

$$c = 2d_{002}$$

This rigorous approach ensures a comprehensive understanding of the tetragonal structure of PSZT-PMI, providing a foundation for further analysis and interpretation of its crystallographic characteristics.

The particle size distribution of each ceramic sample was measured using a Malvern Mastersizer Hydro2000G granulometer, which is capable of measuring grain sizes ranging from 0.02 to 2000 µm. The measurements were conducted in an aqueous medium with the addition of sodium hexametaphosphate as dispersant under agitation and ultrasonic treatment for 15 minutes.

To determine the dielectric properties, such as relative permittivity (ε_r) and dissipation factor (tanδ), the pellets were polished, and silver paste was used to establish ohmic contact on both sides of the samples. Dielectric measurements were recorded during heating over a frequency range of 1 Hz to 1000 kHz at different temperatures (25–500 °C) using an Agilent precision LCR meter (20 Hz–1 MHz). The LCR meter was connected to a computer-controlled temperature chamber. Capacitance values were converted to relative permittivity using the sample geometry and the permittivity of air.[11]

Raman analysis was conducted using a Raman Labram HR800 spectrophotometer, utilizing a diffusing helium ionized ray beam with a wavelength of 633 nm and a spectral resolution of 3 cm^{-1}.

The microstructural properties of the studied ceramics have been investigated by scanning electron microscopy using VEGA 3 TESCAN equipment operating at a voltage of 2 kV under low vacuum. The studied samples have been silver coated prior to analysis.

RESULTS AND DISCUSSION

Figure 1 illustrates the X-ray diffraction (XRD) patterns of the specimens sintered at 1250°C, depicting the variation in Sm content. The characteristic tetragonal phase of perovskite at room temperature is typically distinguished by distinct peaks at approximately 2θ = 22° for (100) and (001), as well as peaks at around 2θ = 45° for (200) and (002). These peak positions indicate that the introduction of Sm dopant does not significantly impact the formation of the tetragonal phase.

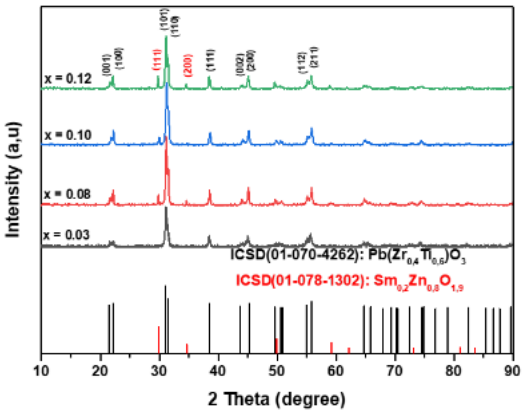

Fig. 1 – XRD patterns of PSZT-PMI sintered at 1250 °C.

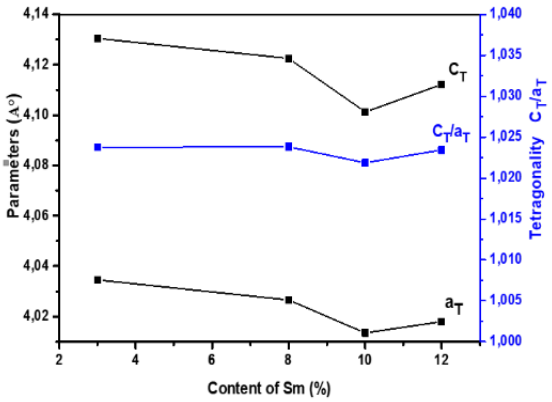

Fig. 2 – Plots of tetragonality vs concentration (mol%) and variation of lattice parameters with concentration (mol%) of different compositions sintered at 1250°C.

Table 2 (see Fig. 2) presents the associated changes in lattice parameter and the degree of tetragonality (*c*/*a*). The calculated values for tetragonality in all the samples suggest that the addition of Sm to PZT-PMI does not cause

significant variations in tetragonality, except for compositions with x = 0.08, 0.10, and 0.12, where an additional peak corresponding to the perovskite (110) plane is observed.[16–17]

This secondary phase has been identified as $Sm_{0.2}Zr_{0.8}O_{1.9}$ based on the PDF2 database (file number 01-078-1302). The relative quantity of the secondary phase in relation to the perovskite phase was estimated using the peak area ratio applying the following equation:[18–19]

$$\text{Secondary phase [\%]} = \frac{I_{SP\,(111)}}{I_{SP(111)}+I_{PZT(110)}} \times 100 \quad (1)$$

Table 2

The lattice parameters, c_T/a_T ratio, relative amount of the secondary phase (SP %), experimental density (D_{exp}), Theoretical density (D_{the}), relative density (D_{rel}) and porosityof PSZT-PMI sintered at 1250 °C.

x %	System (tetragonal)				SP %	D_{exp} (g/cm^3)	D_{the} (g/cm^3)	D_{rel} (g/cm^3)	Porosity (%)
	a_T (Å)	c_T (Å)	c_T/a_T	V(Å^3)					
3	4.03458	4.13048	1.02376	67.23527	0	6.2289	8.0386	77.4873	22.513
8	4.00032	4.09484	1.02362	65.52792	12.67	7.5550	8.1531	92.6641	7.3360
10	4.00910	4.09882	1.00223	65.87985	16.57	7.4573	8.0718	92.3870	7.6130
12	4.01798	4.11218	1.02344	66.38770	18.63	7.3164	7.9725	91.7704	8.2290

The relative amount of the secondary phase exhibits a gradual increase from 0% to 18.63% as the Sm doping level increases. This increase is relatively small and aligns with values reported in doped PZT literature. Therefore, this particular composition can be considered as a single phase, affirming the homogeneous diffusion of Sm^{3+} within the PZT-PMI perovskite structure. The presence of donor ions, Sm^{3+}, leads to partial substitution of Pb^{2+} at the A site, while donor/ acceptor ions Mo^{6+} and In^{3+} partially substitute $Zr4^{+}/Ti^{4+}$ at the B site. This substitution is facilitated by the closely matched and similar ionic radii of the respective cations at the A site and B site in the PZT lattice.

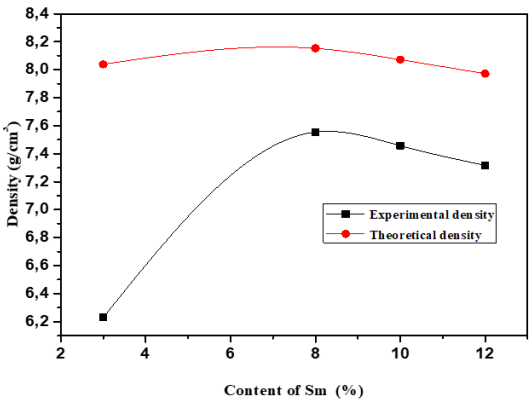

Fig. 3 – The experimental and the theoretical density of PSZT-PMI ceramics sintered at 1250°as a function of the Sm content.

Figure 3 presents the density curves for all the samples sintered at 1250°C, showcasing the relationship between Sm content and both experimental and theoretical density. The experimental density exhibits an increasing trend as the Sm concentration rises, reaching a maximum value of 7.5550 g/cm³ (equivalent to 92.6641% of the theoretical density) at x = 8% (sample No. 2).[20] Subsequently, the density decreases.

The observed increase in density signifies a reduction in the number and size of pores, leading to a more compact structure with a reduced cell volume. Achieving an optimal density depends on various factors, including the addition of impurities, the heating rate, duration of thermal treatment, and the protective atmosphere employed.[21]

Figure 4 illustrates the porosity of the studied samples sintered at 1250 °C as a function of Sm. Notably, the porosity undergoes a decreasing trend until it reaches a minimum value of p = 7.3360 % at x = 0.08 (sample No. 2), after which it begins to increase.

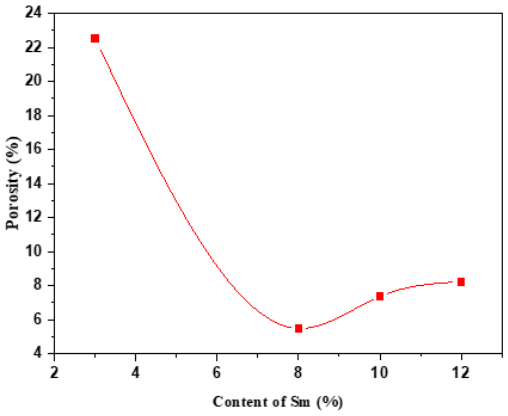

Fig. 4 – The variation of porosity of PSZT-PMI ceramics sintered at 1250°C as a function of the concentration of Sm [%].

Figure 5 depicts the particle size distribution in volume as a function of Sm concentration for the $Pb_{1-x}Sm_x[Zr_{0.50}Ti_{0.45}(Mo1/3In_{2/3})_{0.05}]_{1-x/4}O_3$ powder, considering a sintering temperature of approximately 1250°C. The average diameters in volume, represented as D_v (0.5), are measured to be 0.174 µm, 0.181 µm, 0.181 µm, and 0.179 µm, respectively. These results highlight that composition with 8 % and 10 % of Sm, which exhibit high density values, share the same average grain size. This finding further validates the presence of porosity within their structures.

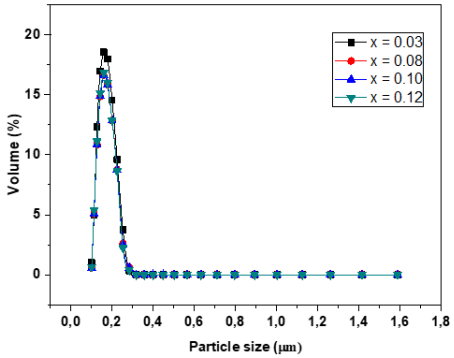

Fig. 5 – Particle size distribution in volume as a function of the concentration of Sm % corresponding to PSZT-PMI ceramics sintered at 1250°C.

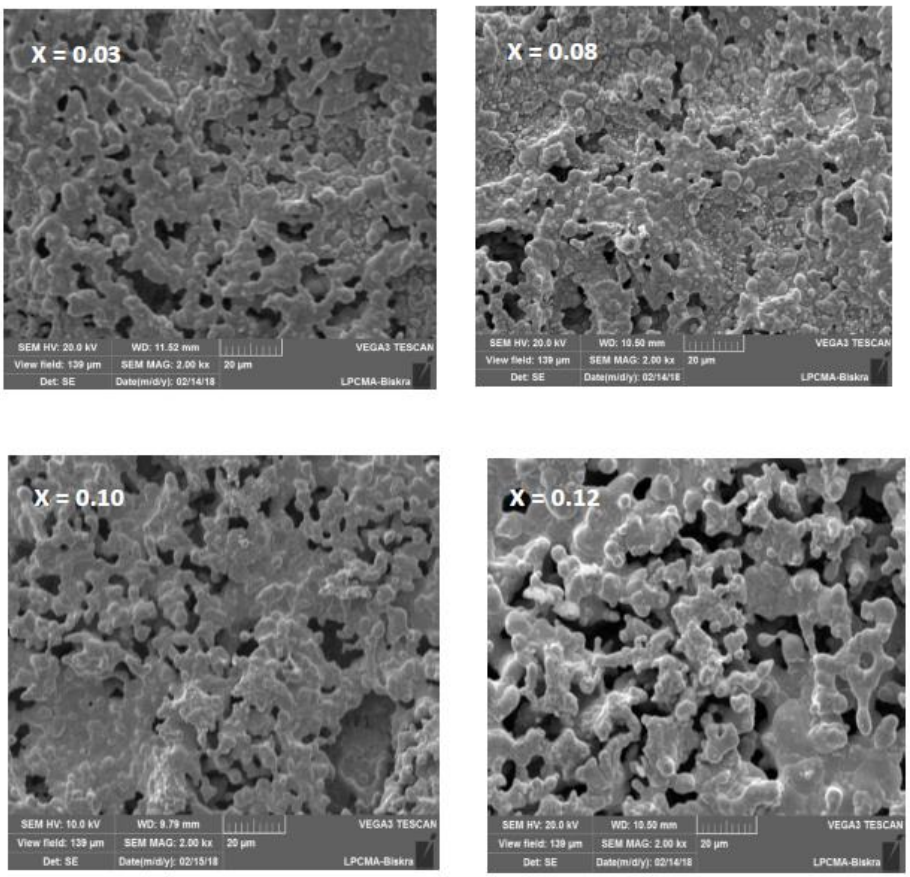

Fig. 6 – SEM images of PSZT-PMI ceramics sintered at 1250°C.

Figure 6 presents the scanning electron micrographs of the ceramics under probe with x = 0.03, 0.08, 0.10, and 0.12, sintering at 1250°C. The micrographs reveal that grains of varying shapes and sizes are uniformly distributed across the entire surface of the samples. This observation signifies a homogeneous distribution of grains throughout the ceramic material. The average grain size in the ceramics was determined directly from the SEM micrographs using the linear interception method, while the density was measured based on the sample geometry.

Figure 7 illustrates the temperature-dependent variation of the dielectric constant for all samples at different frequencies ranging from 1 kHz to 1000 kHz. Notably, the dielectric behavior of the samples exhibits a distinct dielectric peak, characteristic of the ferroelectric to paraelectric phase transition observed in ferroelectric materials.[22] At lower

frequencies, higher values of ε_r are observed, which can be attributed to the simultaneous presence of various types of polarizations such as space charge, dipolar, ionic, and electronic polarizations. However, as the frequency increases, the dielectric constant decreases, indicating the dominance of electronic polarization at higher frequencies.[23]

The temperature at which the dielectric constant reaches its maximum value is known as the Curie or critical temperature (T_c). This temperature corresponds to the phase transition between the ferroelectric and paraelectric phases, making it a crucial parameter.[24] It is worth noting that at high temperatures, the dielectric constant's dependence on frequency is influenced by the contribution of space charge polarization. At lower frequencies, the space charge polarization, arising from charge accumulation at grain boundaries and electrode interfaces, becomes more prominent, but gradually decreases with increasing frequency. The presence of cation and oxygen vacancies contributes to the increased space charge polarization with rising temperature.[25] Furthermore, the highest value of ε_r max is observed for the composition with $x = 0.08$ ($\varepsilon_r = 1250$ at $T_C = 635$ K), indicating its favorable dielectric properties compared to other compositions studied.

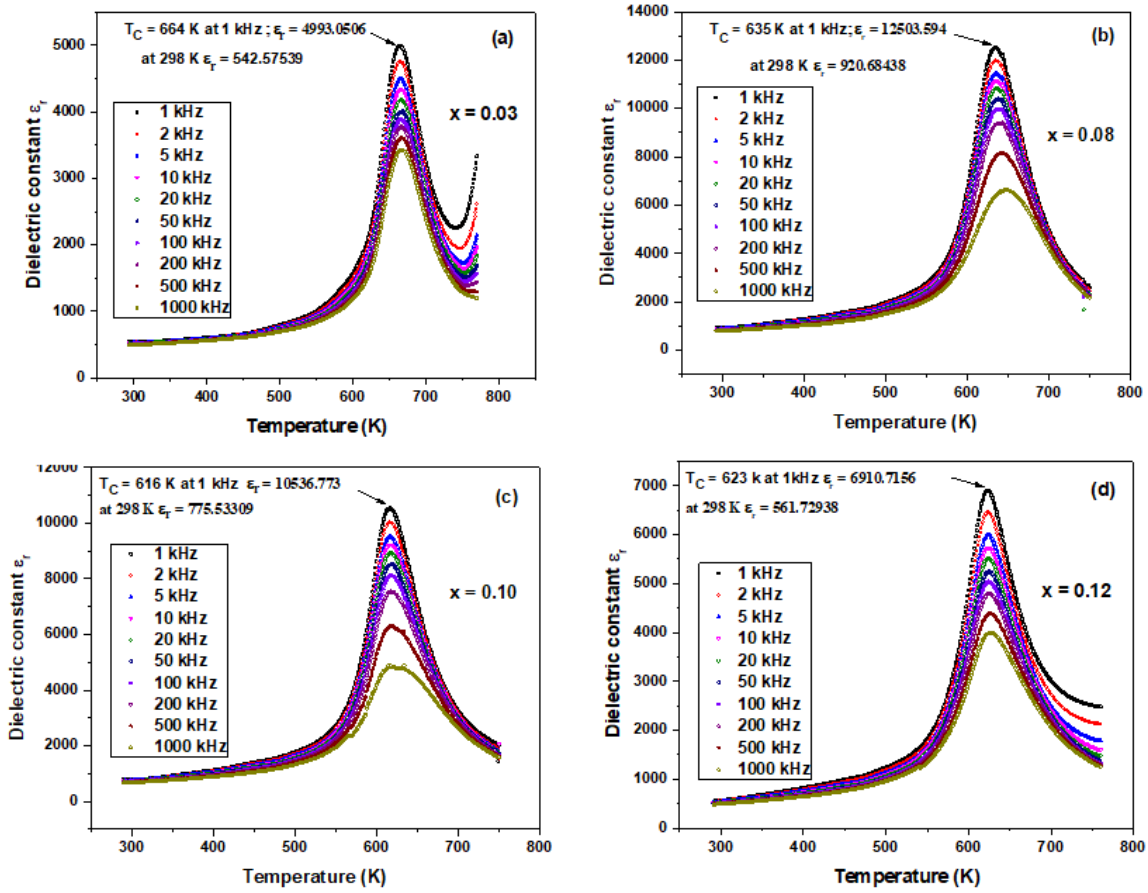

Fig. 7 – Temperature-frequency dependence of relative dielectric constant (ε_r) for PSZT-PMI ceramics sintered at 1250°C.

As can be seen from Fig. 8, the Curie temperature (T_c) exhibits a declining trend as the proportion of Sm increases from $x = 0.03$ to $x = 0.10$. However, an intriguing reversal in this trend is observed when x further increases to $x = 0.12$. This shift in the transition temperature arises from the distortion of the lattice structure and the introduction of defects in charge balance, attributed to the distinct charge and radius of samarium as compared to lead. Similar results have been reported by T. Anil Babu *et al.*[26]

Figure 8 illustrates the temperature dependence of the dissipation factor (tanδ) for compositions with $x = 0.03$, 0.08, 0.10, and 0.12. It is noteworthy that the dielectric loss tangent of all ceramics demonstrates a significant increase at high temperatures, which can be attributed to the phenomenon of thermally activated space charge conduction.[27]

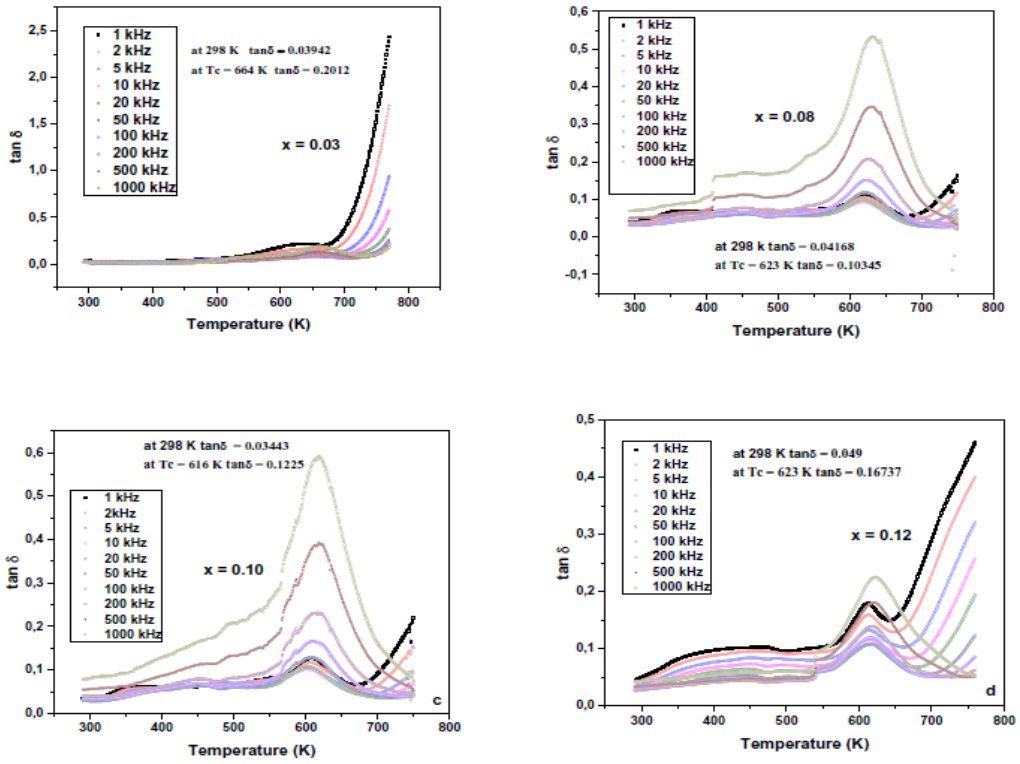

Fig. 8 – Temperature-frequency dependence of tangent loss (tan δ) for PSZT-PMI.

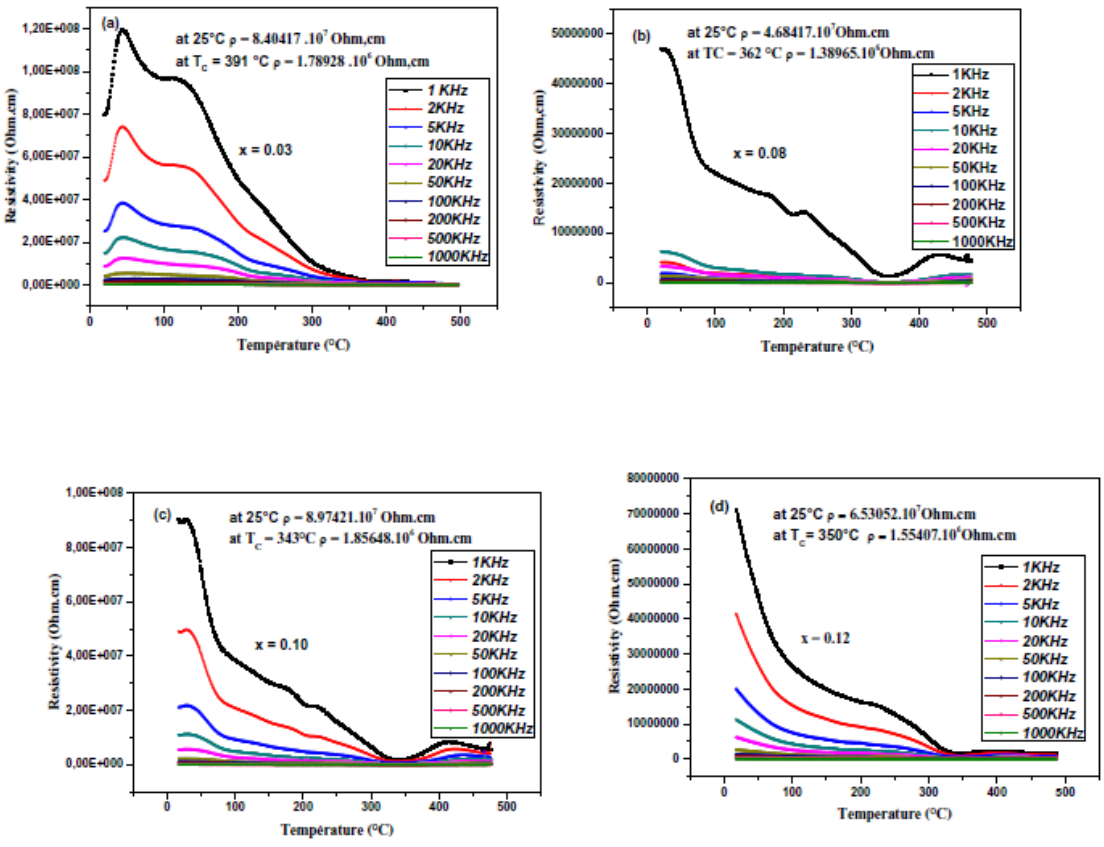

Fig. 9 – Temperature-frequency dependence of resistivity ρ for PSZT-PMI.

To evaluate the electrical properties of our compounds, an investigation of the resistivity was conducted at various temperatures (20–500°C) and frequencies (1kHz–1MHz), as shown in Fig. 9. This study provides insights into the influence of Sm substitution in site A on the electrical behavior. Measuring the resistivity of the doped samples allows for a more comprehensive characterization of their electrical qualities. The resistivity-temperature ($\rho = f(T)$) curves for the compositions within the morphotropic zone are presented. It can be observed that as the temperature increases, the resistivity gradually decreases. This can be attributed to the fact that at higher temperatures, the thermal energy becomes sufficient to disrupt certain ionic or covalent bonds, leading to increased ion mobility.[28,29]

Figure 10 showcases the evolution of $\ln(1/\varepsilon - 1/\varepsilon_m)$ *versus* $\ln(T–T_c)$ at 1 kHz in the temperature range $T > T_c$ (temperature of maximum permittivity) for all the PSZT-PMI ceramics. A remarkable linear relationship is observed between the two logarithmic quantities, regardless of the composition. The diffusivity (γ) of the compounds exhibits a range between 1 and 2, serving as an indicator of the extent of structural disorder in various compounds dependent on specific doping. Systematic calculations of γ values, derived from the slopes of individual curves, have yielded the following results: 1.80978, 1.8078, 1.8003, and 1.38869 for x = 0.03, 0.08, 0.10, and 0.12, respectively. This discerns that the introduction of dopants effectively mitigated disorder within the studied system.

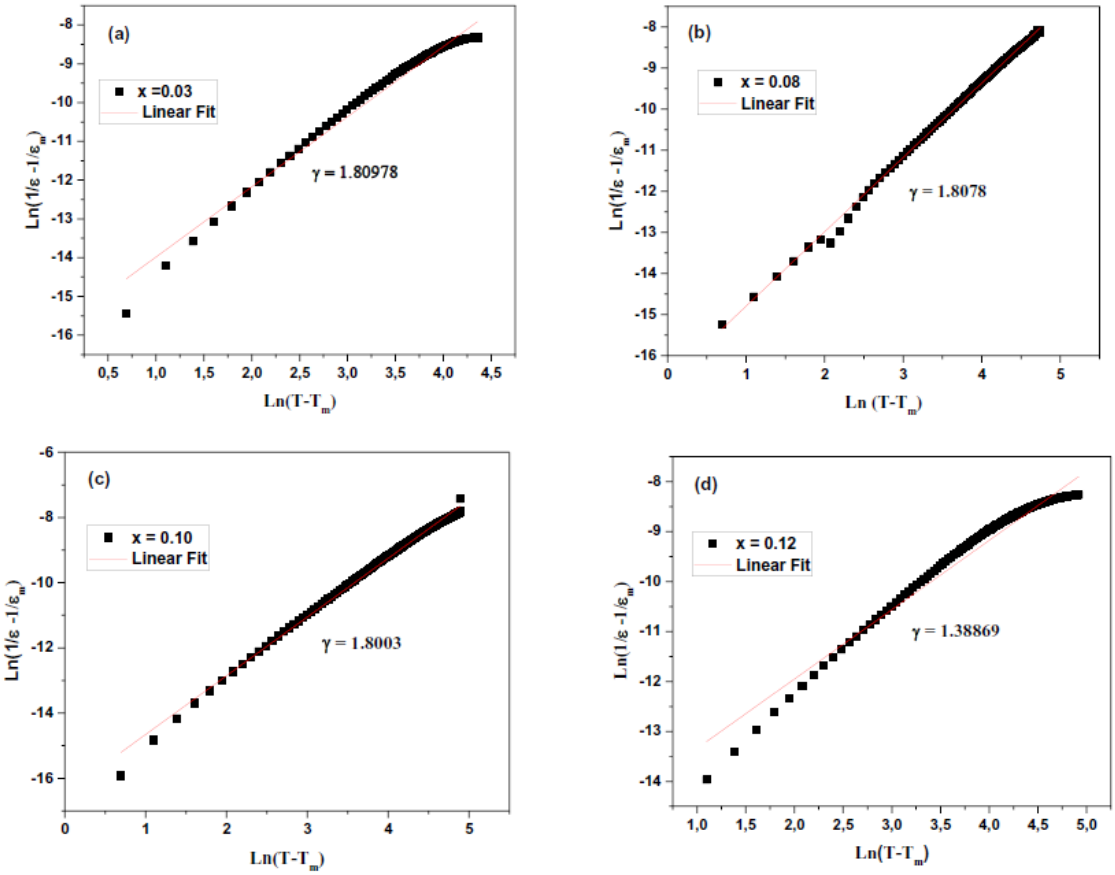

Fig. 10 – Plot of $\ln(1/\varepsilon–1/\varepsilon_m)$ *versus* $\ln(T–T_m)$ for PSZT-PMI ceramics.

Raman spectra of the samples studied, sintered at 1250 °C, are presented in Fig. 11. The E+B1 mode, characteristic of the quadratic symmetry, is observed within the range of 258.2–266.8 cm^{-1} for PSZT-PMI compositions. A1 (3TO) mode, describing the symmetric vibration of O-Ti-O, exhibits a resonance that varies with the strong substitution in the B site of the perovskite structure.[29] Furthermore, the A1 (2TO) mode demonstrates an increase with the rise in sintering temperature. Its presence is attributed to the phase T, as this mode serves as a clear indicator of the appearance of phase T. The Raman spectra also reveal four active modes within the 500–900 cm^{-1}

range, corresponding to the tetragonal structure (T). These modes include the (T) A1 (3TO) mode at 584.6 cm^{-1}, the (T) A1 (3LO) mode at 783.9 cm^{-1}, the (T) E (4TO) mode at 529.8 cm^{-1}, and the (T) E (4LO) mode at 716.8 cm^{-1}.[30]

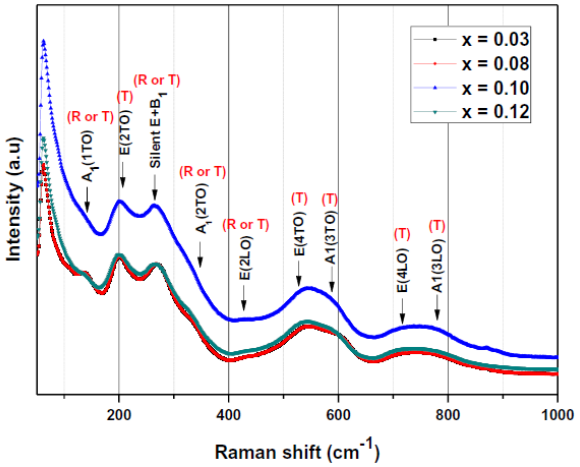

Fig. 11 – Raman spectra of the studied PSZT-PMI ceramics sintered at 1250°C.

CONCLUSION

In this study, a series of $Pb_{1-x}Sm_x[Zr_{0.50}Ti_{0.45}(Mo1/3In_{2/3})_{0.05}]_{1-x/4}O_3$ ceramics (x = 0.03, 0.08, 0.10, and 0.12) were successfully synthesized using conventional mixed oxide ceramic processing techniques. The structural and dielectric properties of the ceramics were systematically investigated. The findings demonstrate that the introduction of samarium Sm into PZT-PMI ceramics results in the preservation of the tetragonal phase. Additionally, it was observed that the addition of small amounts of Sm^{+3} ($x \leq 0.08$) enhances the densification of the ceramics. Among the compositions studied, the sample with x = 0.08 exhibited the most favorable electrical properties, with a high relative permittivity (ε_r) value of 12503.5944 and a low dissipation factor (tanδ) value of 0.04168. These excellent electrical properties make this composition highly promising for applications in actuators.

REFERENCES

1. B. Jaffe, W. R. Cook Jr. and H. Jaffe, "Piezoelectric Ceramics, Academic Press", London and New York, 1971, pp. 1–328.
2. Y. Matsuo and H. Asaki, *J. Am. Ceram. Soc.*, **1965**, *48*, 289–290.
3. E. Quandt and A. Ludwig, Sens. *Actuator A Phys.*, **2000**, *81*, 275–280.
4. R. Zuo, L. Li, X. Hu and Z. Gui, *Mater. Lett.*, **2002**, *54*, 185–190.
5. K. H. Hardtl, *J. Am. Ceram. Soc.*, **1981**, *64*, 283–288.
6. J. S. Kim, K. H. Yoon, B. H. Choi, J. O. Park and J. M. Ma, *Korean Ceram. Soc.*, **1990**, *27*, 187.
7. A.P. Smyth, "Dielectric Behavior and tructure", McGrawHill Publishers, NewYork, USA, 1955, pp. 1–441.
8. G. H. Haertling, *J. Am, Ceram. Soc.*, **1999**, *82*, 797–818.
9. G. H. Haertling, *Ferroelectrics*, **1987**, *75*, 25–55.
10. G. S. Snow, *J, Am, Ceram, Soc.*, **1973**, *56*, 91–96.
11. A. Mirzaei, M. Bonyani and S. Torkian, *Process. Appl. Ceram.*, **2016**, *10*, 175–182.
12. B. Gao, Z. Yao, D. Lai, Q. Guo, W. Pan, H. Hao, M. Cao, H. Liu, *J. Alloys Compd.*, **2020**, *836*, 155474.
13. F. Li, D. Lin, Z. Chen, Z. Cheng, J. Wang, C. Li, Z. Xu, Q. Huang, X. Liao, L.Q. Chen, T.R. Shrout and S. Zhang, *Nat Mater.*, **2018**, *17*, 349–354.
14. L. Shi, P. Wu, L. Yu, Y. Zhao, Z. Li, W. Zhao, Z. Wang, Y. Peng, W. Hua, J. Wang, R. Song and W. Fei, *Ceram. Int.*, **2022**, *48*, 10024–10030.
15. X. Xing and X. Zhu, *J. Wuhan Univ. Technol. -Mat. Sci. Edit.*, **2020**, *35*, 1038–1042.
16. S. R. Shannigrahi, R. N. P. Chaudhary and H. N. Achary, *Mater. Lett.*, **1999**, *39*, 318–323.
17. J. Lian, L.Wang, J. Chen, K. Sun, R. C. Ewing, J. M. Farmer and L. A. Boatner, *Acta Mater.*, **2003**, *51*, 1493–1502.
18. A. Garg and D. C. Agarwal, *Mater. Sci. Engineering: B.*, **2001**, *86*, 134–143.
19. S. I. Swartz and T. R. Shrout, *Mater, Res,Bull.*, **1982**, *17*, 1245–1250.
20. F. Kahoul, L. Hamzioui and A. Boutarfaia, *Energy Procedia*, **2015**, *74*, 184–190.
21. M. Abba, Z. Necira, N. Abdessalem and A. Boutarfaia (Eds.), "Contribution to the study of the coexistence of phases tetragonal-rhombohedral in ceramic type PZT and general form: Pb $[ZrxTi_{0,95-x}(Mo_{1/3}In_{2/3})_{0.05}]O_3$", EPJ Web of Conferences 29, 2012, pp. 1–8.
22. Khushbu, P. Kumar and V. Kumar, *J. Alloys Compd.*, **2018**, *731*, 760–765.
23. M. A. Hilhorst, C. Dirksen, F. W. H. Kampers and R. A. Feddes, *Soil Sci. Soc. Am. J.*, **2000**, *64*, 1581–1587.
24. F. Saouli, F. Z. Sriti, M. Abba, Z. Necira, H. Menasra and A. Beddari, *Ann. Chim.-Sci. Mat.*, **2018**, *42*, 221–231.
25. R. J. Klein, S. Zhang, S. Dou and B. H. Jones, *J. Appl. Phys.*, **2006**, *124*, 144903–144908.
26. T. A. Babu, K. V. Ramesh, T. Badapanda, S. Ramesh, K. C. B. Naidu, D. L. Sastry, *Ceram. Int.*, **2021**, *47*, 31294–31301.
27. R. Yimnirun, S. Ananta and P. Laoratankul, *Mater. Sci. Eng., B, Solid- state Mater. Adv.Technol.*, **2004,** *112*, 79–86.
28. D. S. Keeble, F. Benabdallah, P. A. Thomas, M. Maglione and J. Kreisel, *Appl. Phys. Lett.*, **2013**, *102*, 092903.
29. D. Bauerle and A. Pinczuk, *Solid State Commun.*, **1976**, *19*, 1169–1171.
30. A. Meklid, S. E. Hachani, Z. Necira, H. Menasra, M. Abba and A. Boutarfaia**,** *Appl. Phys. A.*, **2020,** *126*, 1–7.